Ice Shape Analysis of an eVTOL Propeller in Forward Flight at the NASA Glenn Icing Research Tunnel

Paul H. von Hardenberg[1] and Curtis A. Flack[2]
NASA Glenn Research Center, Cleveland, OH, 44135, United States

David L. Rigby[3]
HX5 LLC, Brook Park, OH, 44135

Advanced Air Mobility (AAM) introduces many novel electric vertical takeoff and landing (eVTOL) aircraft configurations for which the effect of icing is not well understood. While icing computational tools have often aided in the design and certification of conventional aircraft, experimental data is needed to support the development and validation of such tools for eVTOL applications. To investigate the icing phenomenon relevant to eVTOL aircraft, NASA Glenn Research Center developed a general-purpose propeller test stand for conducting fundamental icing research on electrically driven propellers in the Icing Research Tunnel (IRT). A 10-day test entry in the IRT was completed in March, 2023, with the goal of generating ice accretions on a non-proprietary propeller geometry under well-characterized conditions. Three carbon fiber propellers of diameters 0.610, 0.711, and 0.914 m (24, 28, and 36 in) were used during the test. Various parametric sweeps of cloud and operating conditions were performed to evaluate the sensitivity of the parameters on the resulting ice accretion characteristics such as ice thickness, mass, location (impingement limits), and type (glaze vs rime). Ice shapes were reviewed for their repeatability, correctness of trends, and sensitivity to parameter variations. The data from the test is being used to support the development of the ice accretion solver, GlennICE.

I. Nomenclature

A_c	=	accumulation parameter
c	=	airfoil chord
D	=	propeller diameter
J	=	advance ratio
n	=	freezing fraction
n_0	=	freezing fraction at stagnation
n_0^*	=	freezing potential at stagnation
N	=	propeller rotational speed, rev/s
r	=	radial distance
R	=	propeller tip radius
$t_{\infty,0}$	=	freestream total air temperature
V_{ax}	=	axial component of air velocity
V_{eff}	=	effective air velocity

[1] Research Aerospace Engineer, Icing Branch, 21000 Brookpark Rd., MS 11-2
[2] Aerospace Flight Systems Engineer, Systems Engineering and Architecture Division, 21000 Brookpark Rd., MS-162-4, AIAA Member
[3] Aerospace Engineer V, 2001 Aerospace Parkway

V_{rot} = rotational component of air velocity
V_∞ = freestream air velocity
We_L = Weber number based on length L
β = collection efficiency
β_0 = collection efficiency at stagnation
δ = drop median volumetric diameter (MVD)
τ = icing time
ω = propeller rotational speed, rad/s

II. Introduction

An emerging aviation industry called Advanced Air Mobility (AAM) is seeking to provide safe, sustainable, and more accessible air transportation services of both people and cargo to augment current ground modes of transportation. From small package delivery drones to larger, passenger-carrying air taxis, AAM is a broad term that encompasses many different vehicle types and mission objectives. Urban Air Mobility (UAM) is a subset of AAM which is focused on localized missions of up to approximately 120 km (75 miles) within and around metropolitan areas [1]. Many electric vertical takeoff and landing (eVTOL) vehicles have been proposed for UAM due to their energy efficiency and ability to take off and land vertically without the need of conventional airports or runways. In contrast with conventional VTOL aircraft, such as helicopters, many of the proposed eVTOL vehicles for UAM have vectored thrust capabilities which is believed to enable more efficient and quiet operations during the cruise phase of flight. An example of a UAM vehicle with vectored thrust capabilities is the NASA tiltwing reference vehicle shown in Fig. 1 [2].

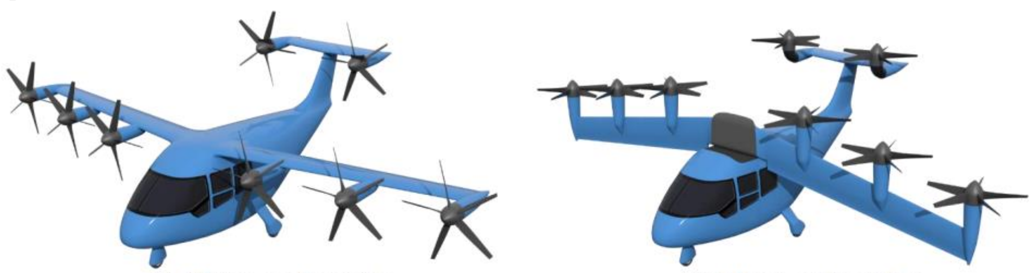

Fig. 1 Renderings of NASA's Tiltwing Reference Vehicle in a Cruise (a) and Hover (b) Configuration

For the AAM industry to be sustainable, it must maintain the high level of safety that defines current commercial aviation. In addition, the scalability of AAM operations will be limited by their ability to operate in inclement weather. Icing is one weather related challenge that presents a significant risk to the safe operation of eVTOL vehicles and the scalability of their operations. As with all aircraft, ice formation on lifting surfaces and propulsors leads to a reduction in lift and thrust, and an increase in drag and stall speed of the vehicle. For continuous flight in icing conditions, most if not all aircraft are equipped with ice protection systems (IPS) that either remove ice or prevent ice from forming in the first place. However, the limited power capacity of many eVTOL aircraft may prohibit the use of a conventional IPS which consumes a significant amount of electrical or thermal energy. At least initially, many eVTOL manufacturers will likely not seek certification for flight into known icing (FIKI) in part for this reason. However, icing certification may be a longer-term objective for eVTOL manufacturers who wish to enable all-weather operations of their vehicles and minimize operational downtime due to unfavorable weather conditions, such as icing.

Regardless of whether an eVTOL manufacturer intends to certify their vehicle for FIKI, they will likely need to demonstrate safe operation during an inadvertent icing encounter for a limited time as complete avoidance of icing conditions cannot be guaranteed. In 2024, the FAA announced the special class airworthiness criteria for both the Joby Aero, Inc. (Joby) Model JAS4-1 and the Archer Aviation, Inc. (Archer) Model M001 powered-lift eVTOL which requires the applicants to "provide a means to detect icing conditions for which certification is not requested and show the aircraft's ability to avoid or exit those icing conditions" [3,4]. However, due to the novelty of eVTOL aircraft, it remains to be seen how eVTOL manufacturers will demonstrate compliance with these requirements. While icing analysis tools have often aided in the design and certification of many conventional aircraft, no such tool has been validated or developed specifically for eVTOL configurations. As such, experimental data is needed not only to better understand the icing risks relevant to eVTOL aircraft, but also to provide validation data for the development of icing analysis tools to aid during certification and design.

To investigate the icing phenomenon relevant to eVTOL aircraft, NASA Glenn Research Center developed a general-purpose propeller test stand for conducting fundamental icing research on electrically driven propellers in the Icing Research Tunnel (IRT). A 10-day test entry in the IRT was completed in March, 2023, with the goal of generating ice accretions on a non-proprietary propeller geometry under well-characterized conditions. Three carbon fiber propellers of diameters 0.610, 0.711, and 0.914 m (24, 28, and 36 in) were used during the test. All three propellers had a NACA 0012 airfoil geometry and were geometrically scaled from a radial location of roughly r/R = 0.40 to r/R = 1.0. Various parametric sweeps of cloud and operating conditions were performed to evaluate the sensitivity of the parameters on the resulting ice accretion characteristics such as ice thickness, mass, location (impingement limits), and type (glaze vs rime). Propeller performance degradation in the form of torque change over time was also captured during each run. Several ice shedding events were captured using a high-speed camera from which important shedding characteristics such as shedding time and location could be determined.

This paper provides an analysis and discussion of the experimental ice shapes obtained during the test. The data obtained during this test will be used to develop and validate icing computational tools, such as GlennICE, which predicts the onset and growth of ice [5]. A complimentary paper by Rigby and von Hardenberg [6] provides the results of GlennICE simulations performed on the three propeller sizes tested during this effort.

III. Test Article and Instrumentation

A. Propeller Test Stand

A picture of the propeller test stand installed in the IRT test section with the 0.914 m (36 in) diameter blades is shown in Fig. 2.

Fig. 2 NASA's eVTOL Propeller Test Stand for Fundamental Icing Studies

The propeller is driven by an EMRAX 188 permanent magnet synchronous motor (PMSM) with a continuous power rating of up to 34 kW (45 hp). The motor has an IP65 ingress protection rating and is liquid cooled to prevent the motor from overheating during operation. The motor comes internally equipped with a type KTY 81-210 temperature sensor for motor temperature measurements. A triaxial accelerometer is mounted directly behind the motor to ensure that safe vibration levels are not exceeded during operation.

A Cascadia Motion CM200DX Inverter converts the output from a DC power supply into 3-phase AC power to drive the motor. The inverter provides an estimate of motor torque based on the power being supplied to the motor and the speed at which the motor is operating. For this test entry, the inverter was set to a speed control mode where a target motor revolutions per minute (RPM) was maintained throughout the duration of the test run.

To measure propeller forces and moments, the test article is compatible with any of the Interface 6A68 6-axis load cells which can be mounted directly aft of the motor as shown in Fig. 3. For this test entry, only the 6A68C model load cell was available. However, conservative estimates of imbalance due to ice shedding at the target motor speeds for this test resulted in bending moments that exceeded the capacity of the 6A68C load cell. Instead, a stainless-steel, cylindrical block of identical dimensions and the same mounting pattern as the 6A68C load cell was fabricated and used as a substitute for the load cell during the test. As a result, no thrust measurements were obtained during the test and all torque measurements came directly from the inverter-estimate of motor torque. While the accuracy of the inverter-estimated torque is not clear, it was found to produce consistent, repeatable results as it was not susceptible to many sources of error common in load cells such as creep, hysteresis, and thermal drift. As such, it was deemed acceptable to use for establishing general trends and relationships between torque and other parameters during this test entry.

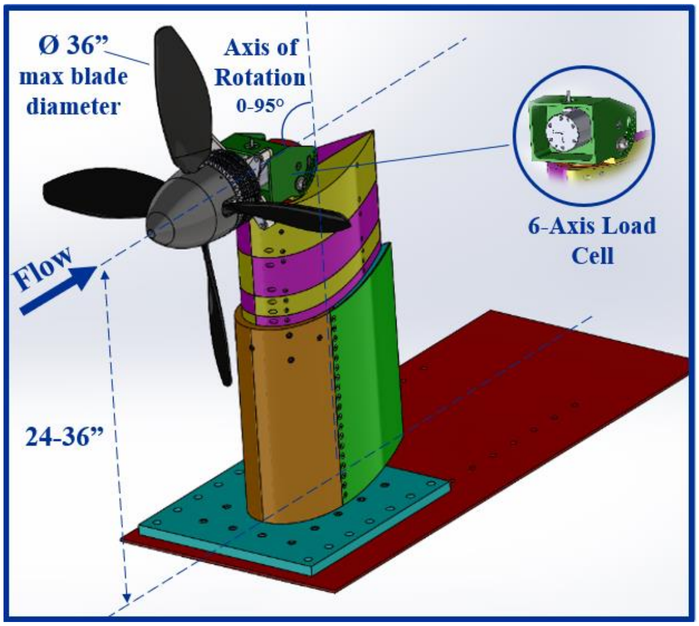

Fig. 3 CAD Model of the Propeller Test Stand Showing Location of Load Cell

The angle between the propeller axis of rotation and the freestream air velocity, known as the propeller incidence angle, can be articulated from 0° (axial flow) to 95° in increments of 5° by adjusting the pitch head on the test stand. The pitch head can also be traversed vertically from 0.61 m (24 in) to 0.91 m (36 in) from the test section floor. This allows the center of rotation of the propeller to remain near the centerline of the test section where the cloud is the most uniform regardless of the pitch head angle setting. The strut, which provides the main structural support of the test stand, is enclosed by a NACA 0040 airfoil for improved airflow characteristics. For this test entry, the propeller remained in an axial-flow configuration to simulate an eVTOL propeller in forward flight. The center of rotation of the propeller was located 0.91 m (36 in) from the floor at the centerline of the test section.

B. Propeller Geometry

Three carbon fiber propellers of diameters 0.610, 0.711, and 0.914 m (24, 28, and 36 in) were custom-made for the 2023 test entry. To maximize data dissemination, a non-proprietary propeller geometry inspired by the Computationally Optimized Proprotor (COPR) design developed by NASA was used [7]. It should be noted, though, that the nominal COPR twist and chord distributions were adjusted for manufacturing feasibility purposes, and so the final design of the propeller blades used for this experiment are not perfect representations of the original COPR design. This was deemed acceptable, however, as the specific design of the propeller was not considered critical for this test entry as long as the geometry remained non-proprietary. The final twist and chord distributions of the three propellers used during this experiment are shown in Fig. 4.

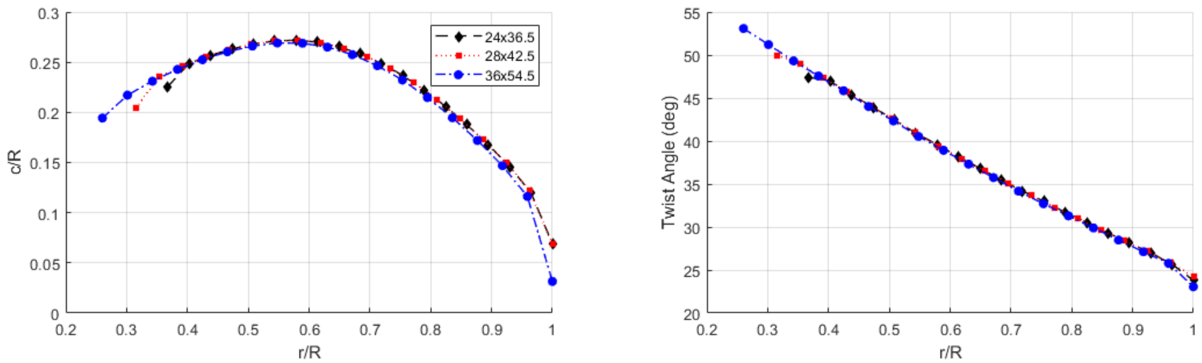

(a) Chord Distributions **(b) Twist Angle Distributions**

Fig. 4 Comparisons of the propeller chord (a) and twist angle (b) distributions between the three propeller sizes.

It can be seen from Fig. 4 that the three propellers have similar normalized twist and chord distributions from a radial location of approximately r/R = 0.40 to r/R = 1.0. The use of the same hub and spinner for each set of propeller blades prevented geometric similarity towards the root of the blade. In the complimentary paper by Rigby and von Hardenberg, the effect of not geometrically scaling the spinner with propeller size was explored using GlennICE and found to have a negligible effect on the predicted ice accretion [6].

A 4-bladed, variable pitch hub was chosen for this test entry to provide greater flexibility in propeller operating conditions. A pitch-adjustment tool was provided by the propeller manufacturer to change the collective pitch of the blades. For this test entry, the target pitch setting for each propeller was increased by 18° from the design twist distributions shown in Fig. 4b. It should be noted, though, that the decision to use a variable pitch hub inevitably comes with some uncertainty in the blade pitch setting. After evaluating the clean scans of the propeller blades obtained during the test, it was determined that the blade pitch angle could deviate as much as one degree from the target pitch setting. Future tests will utilize a calibrated inclinometer to provide more consistent pitch settings.

IV. Test Facility and Procedures

A. Icing Research Tunnel

The tests were performed in the NASA Glenn Icing Research Tunnel [8]. The IRT is a closed-loop, refrigerated, sea level tunnel with a test section size of 1.8 x 2.7 m (6 x 9 ft). The icing cloud is generated by operating 10 spray bars upstream of the test section. The calibrated speed range of the IRT is from 50 to 300 knots (empty) [9]. Ballistic panels were installed on the walls of the tunnel test section to protect personnel in the control room during operation of the propeller. A Phantom v2640 high-speed camera was installed above the test section and upstream of the propeller test stand to capture ice shedding events.

B. Icing Test Procedure

A typical run consisted of incrementally increasing the propeller RPM followed by tunnel speed up to the target conditions for that run. The increments at which the propeller RPM and tunnel speed increased were chosen such that the propeller avoided a windmilling condition which could potentially damage electronic hardware due to the reverse flow of electrical power (a brake resistor was later installed near the end of the test entry which could dissipate the power generated during a windmilling scenario). The incremental approach also allowed for system health checkouts to be performed before moving to a higher speed condition. Once the target propeller RPM and tunnel speed were reached, the tunnel operators would wait until the tunnel was stable at the target tunnel temperature before initiating the spray. During the spray, model vibrational loads were monitored to ensure that the safe operating limits were not exceeded. Once the desired test duration was achieved for that run, the spray was turned off and a similar incremental approach was conducted to reduce the propeller and tunnel speed, this time starting with a decrease in tunnel speed followed by propeller RPM. Once the propeller was completely stopped, researchers entered the test section to document the ice accretion. The documentation process included taking various still images of the model, scanning of ice shapes, and collecting ice mass measurements. It was assumed that there would be little blade to blade variation in ice shape and so only one blade was scanned per run. Each blade was numbered to ensure that the same blade was scanned every time. Afterwards, the ice from the scanned blade was scraped into a bucket and weighed. The spinner, which could be quickly removed from the model via four screws, was weighed after each run to document the spinner ice mass. Finally, any remaining ice was removed from the model using isopropyl alcohol and prepped for the next run.

C. Calculation of Icing Similarity Parameters

The limited test section size and cloud capabilities of the IRT often prevents testing of full-scale models at the desired conditions. In these situations, the use of icing scaling methods provides a methodology to obtain information about the reference model using scaled test conditions. In addition, researchers can manipulate the icing similarity parameters to isolate certain phenomena or investigate the relative sensitivity of different parameters on the resulting ice accretion. A list of the key icing similarity parameters and their descriptions can be found in Table 1.

Table 1 Description of Important Icing Similarity Parameters

Parameter	Variable	Description
Freezing Fraction	n	Fraction of water flux entering a control volume that freezes within the control volume.
Collection Efficiency	β	Fraction of the freestream droplet concentration that impinges on a surface.
Accumulation Parameter	A_c	Theoretical maximum leading edge ice thickness normalized by the airfoil leading edge nose diameter of curvature.
Weber's Number	We_L	Ratio of the inertial forces acting on a drop to its surface tension.

While icing scaling methods for unprotected fixed airfoils have been well established [10, 11], there is no accepted method for scaling icing on rotating airfoils. One approach, which was explored during this study, is to divide the blade into a discrete number of radially distributed sections to which the current recommended icing scaling methods developed for fixed wings can be applied. To calculate the key icing similarity parameters at a given radial location, one must first determine the effective velocity, V_{eff}, that the propeller experiences at that radial location. Due to the rotation and forward airspeed of the propeller, the blade experiences both an axial and rotational component of velocity (V_{ax} and V_{rot}, respectively) which varies radially along the blade. The V_{eff} that the blade experiences at a given radial location can be determined by calculating the resultant magnitude of the V_{ax} and V_{rot} components of velocity at that location as seen in Eq 1.

$$V_{eff} = \sqrt{(V_{ax})^2 + (V_{rot})^2} \tag{1}$$

For this study, it was assumed that the effects of propeller induction could be ignored such that $V_{ax} \approx V_\infty$ and $V_{rot} \approx \omega r$, where V_∞ is the freestream air velocity, ω is the rotational speed of the propeller in rad/s, and r is the distance from the center of rotation to the radial location of interest. With these assumptions, an approximation for V_{eff} can be obtained using Eq. 2. For more accurate values of V_{eff}, blade element momentum theory (BEMT) or computational fluid dynamics (CFD) can be used.

$$V_{eff} \approx \sqrt{(V_\infty)^2 + (\omega r)^2} \tag{2}$$

Once a value for V_{eff} is determined at a given radial location, the key icing similarity parameters can be estimated by substituting V_{eff} for V_∞ during the derivations of those parameters [10, 11].

Another important non-dimensional parameter for propellers is the advance ratio, J, which describes the relationship between the forward airspeed of the propeller and its rotational rate. Matching this parameter is required for flow-field similarity of geometrically similar propellers at the same pitch setting. The formula for advance ratio used in this paper is provided in Eq. 3 where N is the rotational rate of the propeller in rev/s and D is the diameter of the propeller. Note that it was decided to denote the propeller speed in rev/s using a capital letter "N" instead of a lowercase letter "n" as commonly used in propeller aerodynamics. This was done to differentiate the propeller speed from the freezing fraction, n.

$$J = \frac{V_\infty}{ND} \tag{3}$$

In the following section, several ice shapes will be presented along with the corresponding icing similarity parameters that were estimated using the approach described above. For simplicity, only the values calculated at the r/R = 0.75 location are presented for each run condition. Note that, while the freezing fraction has a theoretical limit of unity, calculation of freezing fraction can result in values larger than unity. For this paper, it was decided to present the unbounded values of freezing fraction which will hereinafter be referred to as the freezing potential, n_0^*, with the subscript 0 signifying that it was calculated at stagnation. For values greater than unity, n_0^* provides a way to assess the confidence that a given set of conditions will result in rime ice. For example, a predicted value of n_0^* = 1.80 has a higher degree of confidence that the ice will be rime than a n_0^* = 1.10. As will be seen later in the paper, presenting the unbounded values of freezing fraction will also serve useful when assessing the accuracy of the calculated values of freezing fraction.

While only the values of n_0^* calculated at r/R = 0.75 will be presented for each run condition, Fig. 5 provides an example of how n_0^* varied radially along the span of the blade for three runs which differ only by the freestream total air temperature. For a propeller with a constant chord distribution, n_0^* is expected to be the lowest at the tip of the blade where the propeller experiences the highest V_{eff}. However, due to the tapering chord of the propeller used in this experiment, n_0^* was found to increase towards the tip of the blade. As a result, the lowest value of n_0^* tended to occur between r/R = 0.70 and r/R = 0.80.

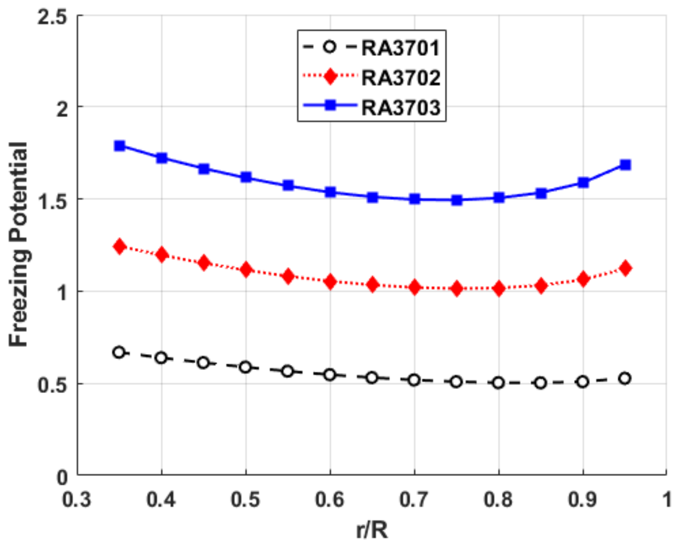

Fig. 5 Example Freezing Potential vs Span Distributions for Runs RA3701, RA3702, and RA3703.

V. Test Data

A. Test Conditions

A total of 45 icing runs were completed. A parametric approach to the test matrix was conducted to better understand the relative importance and sensitivity of key icing parameters and propeller operating conditions on the resulting ice accretion. For this test, the median volumetric diameter (MVD) ranged from 15 to 80 μm, the liquid water content (LWC) ranged from 0.55 to 1.20 g/m^3, the total air temperature ranged from -3 to -15°C, and the icing time ranged from 1.4 to 10 mins. The propeller helical tip speeds for this test ranged from 68.5 to 107.6 m/s, and the advance ratios ranged from 2.32 to 2.71. Of the three propeller sizes, the 28 in diameter propeller accounted for 39 of the 45 total test runs. This paper provides ice accretion data for 21 of the 45 total test runs.

B. Ice Shape Repeatability

Since one of the objectives of this study was to evaluate the relative effects of various parameters on the resulting ice accretion on the propeller, it was important to understand what level of variation could be expected due to normal run to run variations in the cloud conditions. As such, one of the goals of the test was to assess the repeatability of the ice shapes. Figure 6 shows a comparison of three ice shapes that were obtained at the same target cloud and operating conditions. Runs RA3683 and RA3687 were conducted at the start and end of the same day, respectively. Run RA3714 was conducted the following week. As seen from Fig. 6, excellent ice shape repeatability was achieved. Other repeat conditions showed similar levels of repeatability.

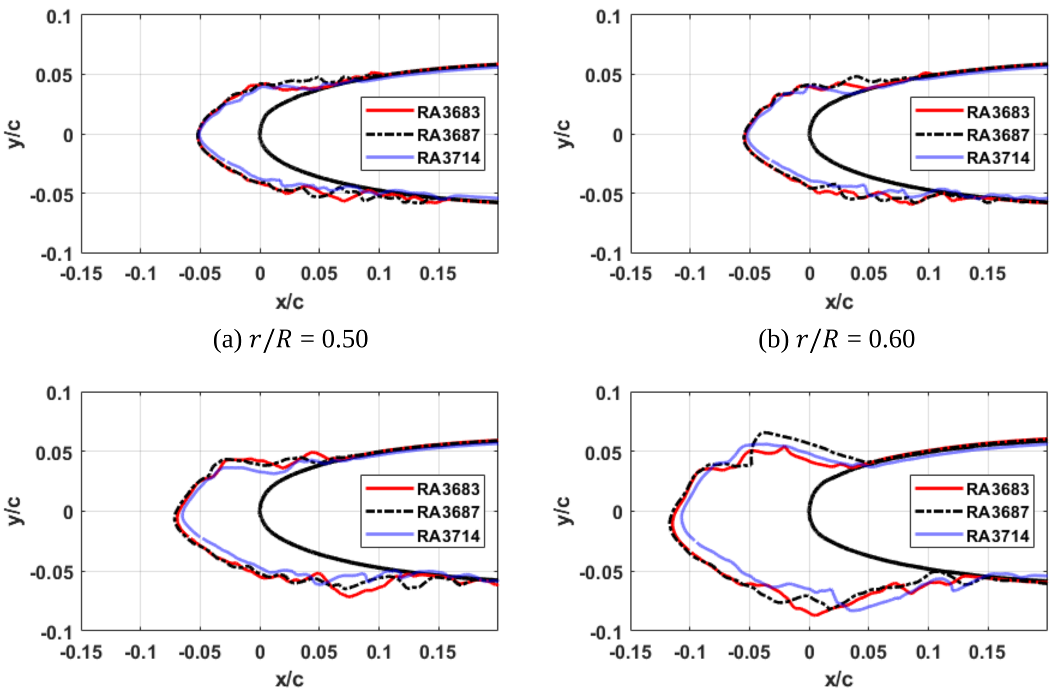

(a) r/R = 0.50 (b) r/R = 0.60

(c) r/R = 0.75 (d) r/R = 0.90

Fig. 6 Ice Shape Repeatability

Table 2 Target Test Conditions for Ice Shape Repeatability

	Target Operating and Cloud Conditions								Similarity Parameters (calculated at r/R = 0.75)				Ice Mass	
Run	V_∞ knots	$t_{\infty,0}$ °C	δ µm	LWC g/m^3	τ min	RPM rev/min	D in	J	n_0^*	A_c	β_0	We_L 10^6	Blade g	Spinner g
RA3683	87	-15.0	15	0.55	3.0	1516	28	2.49	2.37	2.59	0.88	0.15	9.0	10.6
RA3687	“	“	“	“	“	“	“	“	“	“	“	“	8.5	10.3
RA3714	“	“	“	“	“	“	“	“	“	“	“	“	9.8	10.8

C. Effect of Temperature

Temperature is an important parameter that can significantly alter the ice accretion due to its effect on freezing fraction. In general, warmer temperatures tend to promote the formation of glaze ice (n_0 < 1.0) whereas colder temperatures tend to form rime ice (n_0 = 1.0). Figure 7 shows the effect of varying the freestream total air temperature, $t_{\infty,0}$, from -3.0 to -7.5°C.

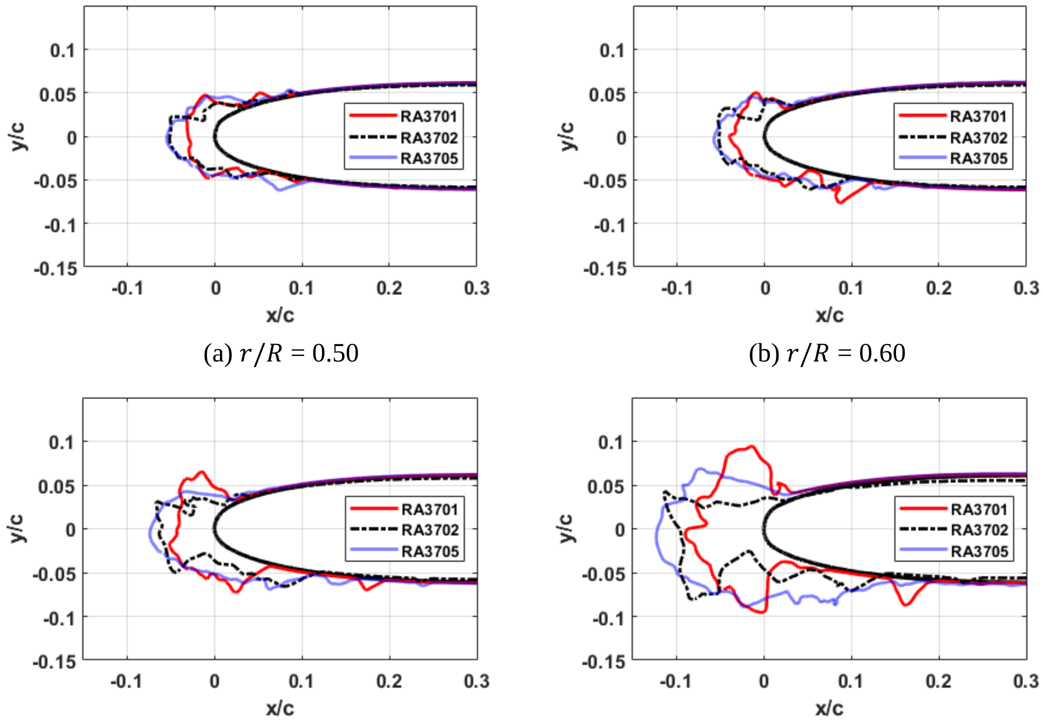

(a) r/R = 0.50 (b) r/R = 0.60

(c) r/R = 0.75 (d) r/R = 0.90

Fig. 7 Effect of Varying Temperature

Table 3 Target Test Conditions for Effect of Varying Temperature

	Target Operating and Cloud Conditions								Similarity Parameters (calculated at r/R = 0.75)				Ice Mass	
Run	V_∞ knots	$t_{\infty,0}$ °C	δ μm	LWC g/m^3	τ min	RPM rev/min	D in	J	n_0^*	A_c	β_0	We_L 10^6	Blade g	Spinner g
RA3701	87	-3.0	15	0.55	3.0	1516	28	2.49	0.51	2.59	0.88	0.15	7.0	8.4
RA3702	"	-6.0	"	"	"	"	"	"	1.01	"	"	"	8.3	9.3
RA3705	"	-7.5	"	"	"	"	"	"	1.26	"	"	"	9.7	10.1

As seen from Fig. 7, the main ice shape changes significantly with decreasing temperature due to the differences in freezing fraction at these temperatures. At -3.0°C, the main ice shape features are consistent with low freezing fractions such as having smaller ice thicknesses and larger horn angles. At -6.0°C, the features of the main ice shape are still consistent with glaze but indicate a higher freezing fraction due to the larger ice thicknesses and smaller horn angles. This is contrary to what was predicted based on the analytical value of n_0^* which was estimated to be 1.01 at -6.0°C as seen in Table 3. By -7.5°C, the predicted n_0^* was 1.26 and the main ice shape showed features more consistent with rime ice. Based on these results, it was concluded that the analytical values of n_0^* were overestimating the true freezing fraction by as much as 0.25 at these conditions.

To ensure the ice was fully rime by -7.5°C, the temperature sweep was continued down to -15°C. As seen from Fig. 8, decreasing the temperature beyond -7.5°C resulted in little to no change in the main ice shape, providing greater confidence that the ice was effectively rime by -7.5°C.

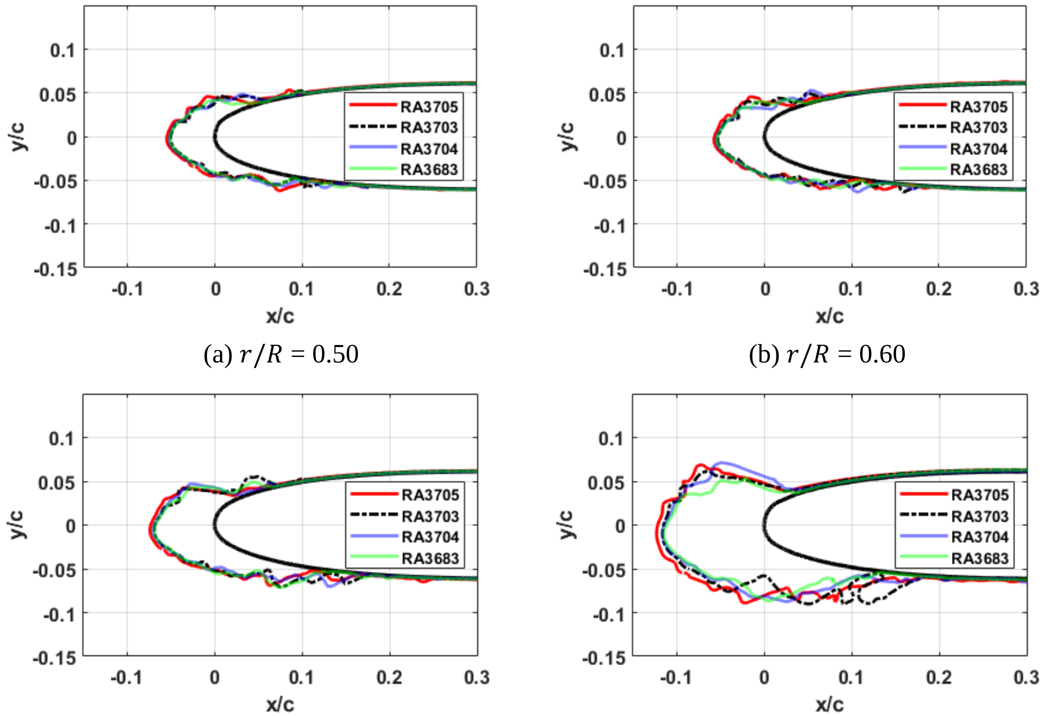

(a) r/R = 0.50
(b) r/R = 0.60
(c) r/R = 0.75
(d) r/R = 0.90

Fig. 8 Effect of Varying Temperature (continued)

Table 4 Target Test Conditions for Effect of Varying Temperature (continued)

Run	Target Operating and Cloud Conditions								Similarity Parameters (calculated at r/R = 0.75)				Ice Mass	
	V_∞ knots	$t_{\infty,0}$ °C	δ µm	LWC g/m^3	τ min	RPM rev/min	D in	J	n_0^*	A_c	β_0	We_L 10^6	Blade g	Spinner g
RA3705	87	-7.5	15	0.55	3.0	1516	28	2.49	1.26	2.59	0.88	0.15	9.7	10.1
RA3703	“	-9.0	“	“	“	“	“	“	1.49	“	“	“	8.7	9.8
RA3704	“	-12.0	“	“	“	“	“	“	1.94	“	“	“	9.1	9.8
RA3683	“	-15.0	“	“	“	“	“	“	2.37	“	“	“	9.0	10.6

While the ice shapes indicated that the ice was effectively rime at -7.5°C, visual observations of the ice accretion revealed a glossy, semi-transparent appearance along the leading edge which would suggest a freezing fraction less than unity as seen in Fig. 9c. As the temperature decreased beyond -7.5°C, the leading edge ice accretion became less glossy and more opaque. By -15°C, the ice accretion had become fully opaque and had no glossy appearance as seen in Fig. 9f.

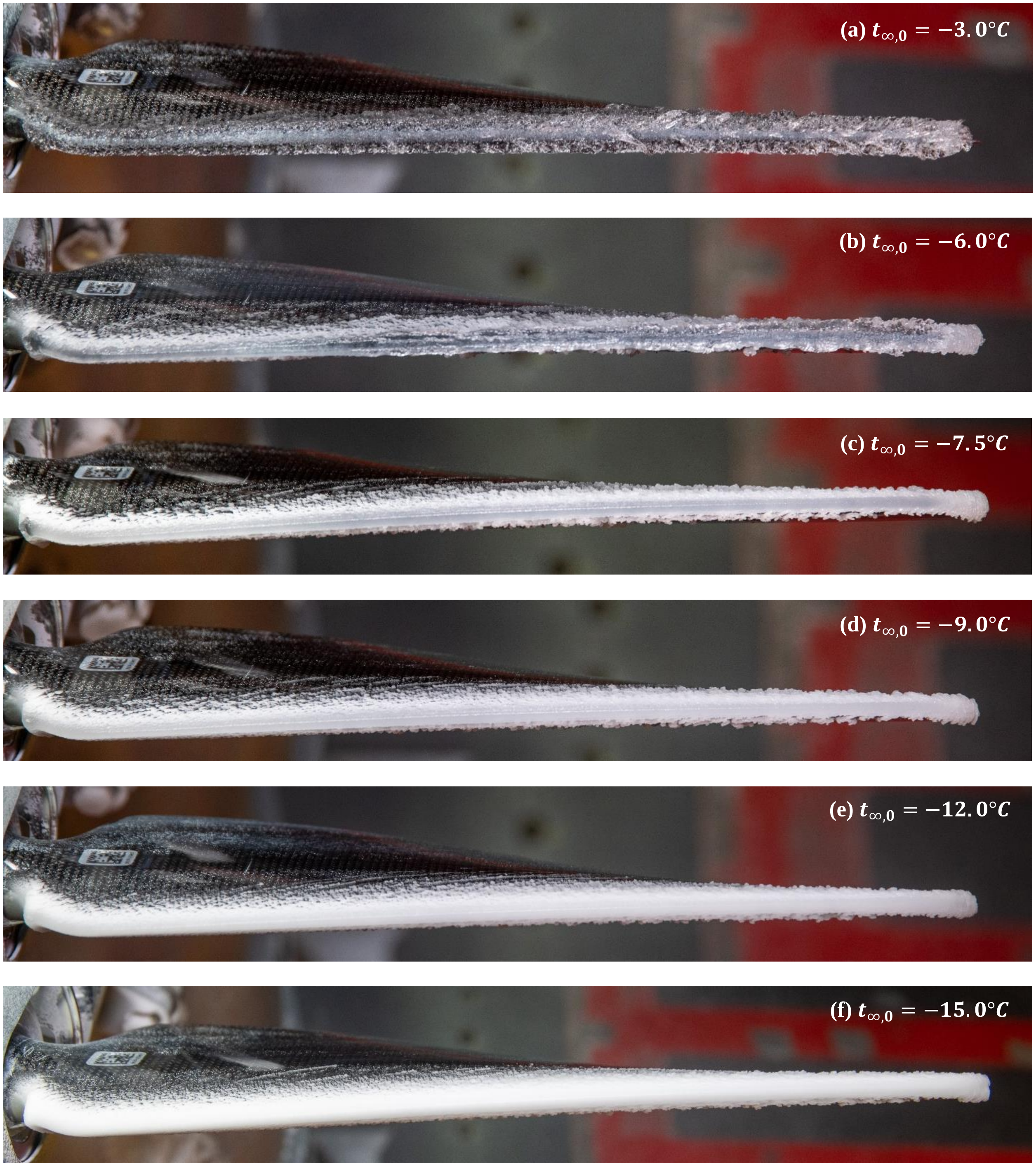

Fig. 9 Photographs of Ice Accretion along Propeller Leading Edge Obtained at $t_{\infty,0}$ of (a) -3.0, (b) -6.0, (c) -7.5, (d) -9.0, (e) -12.0, and (f) -15°C corresponding to runs RA3701, RA3702, RA3705, RA3703, RA3704, and RA3683, respectively.

D. Effect of Icing Time

One aspect of the ice accretion process that makes it particularly challenging to predict is that it effectively alters the geometry of the airfoil with time. As the airfoil surface changes, so too does the flow field around the airfoil which influences the trajectory and impingement of subsequent water droplets. For rime or very short accretion times, the ice shapes will typically follow the contour of the airfoil surface and the changes to the flow field and local collection efficiencies are minimal. For glaze or longer accretion times, the ice shapes may not conform to the original airfoil surface and may have a larger influence on the collection of subsequent water droplets leading to more complicated ice shapes.

To capture how the main ice shape changes with time, two time sweeps were performed. The first time sweep was performed at rime conditions for icing times of 1.5, 3.0, 4.5, and 6.0 mins as seen in Fig. 10. Note that the ice was removed from the propeller after each run before repeating the run at the next time interval. As expected, the shortest icing exposure shows the best agreement with the original profile of the airfoil. Note that run RA3695 experienced an ice shedding event which occurred somewhere between r/R = 0.75 and r/R = 0.90 of the scanned blade as seen in Fig. 10d.

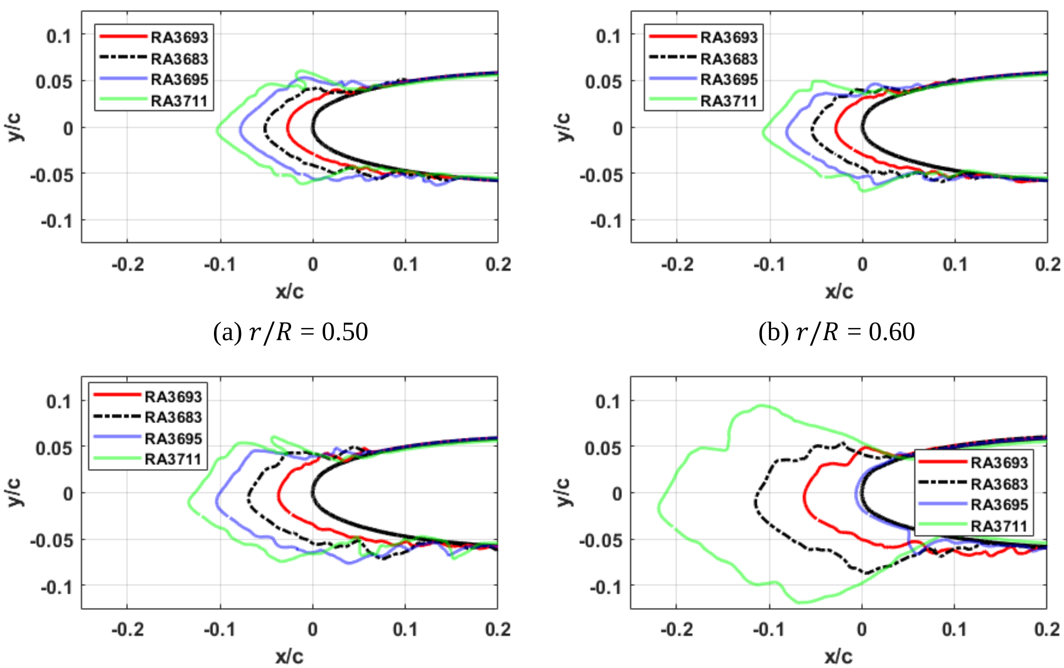

(a) r/R = 0.50 (b) r/R = 0.60

(c) r/R = 0.75 (d) r/R = 0.90

Fig. 10 Effect of Icing Time (n_0 = 1)

Table 5 Target Test Conditions for Effect of Icing Time (n_0 = 1)

	Target Operating and Cloud Conditions								Similarity Parameters (calculated at r/R = 0.75)				Ice Mass	
Run	V_∞ knots	$t_{\infty,0}$ °C	δ μm	LWC g/m^3	τ min	RPM rev/min	D in	J	n_0^*	A_c	β_0	We_L 10^6	Blade g	Spinner g
RA3693	87	-15.0	15	0.55	1.5	1516	28	2.49	2.37	1.30	0.88	0.15	4.2	5.1
RA3683	"	"	"	"	3.0	"	"	"	"	2.59	"	"	9.0	10.6
RA3695	"	"	"	"	4.5	"	"	"	"	3.89	"	"	10.7*	15.9
RA3711	"	"	"	"	6.0	"	"	"	"	5.18	"	"	21.0	21.5

*Ice mass affected due to shedding

The second time sweep was performed at glaze conditions for icing times of 1.4, 2.1, and 2.8 mins as seen in Fig. 11. The icing times for the glaze conditions were chosen to match the A_c of the latter three runs during the rime time sweep to account for the difference in LWC. As seen from Fig. 11, the ice shapes quickly diverge from the original airfoil contour due to the formation of horns.

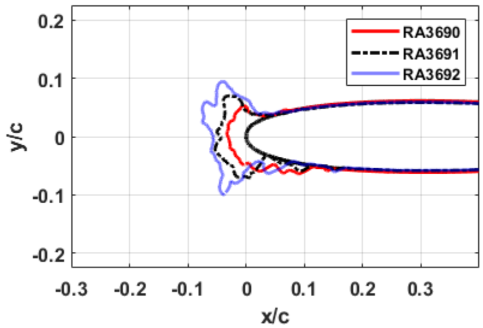

(a) r/R = 0.50

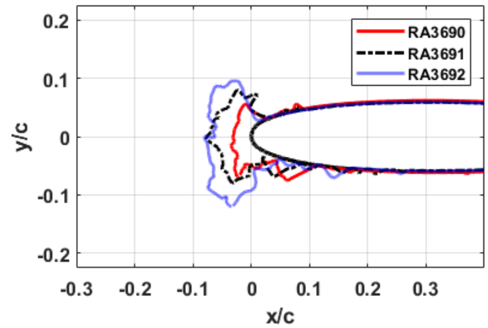

(b) r/R = 0.60

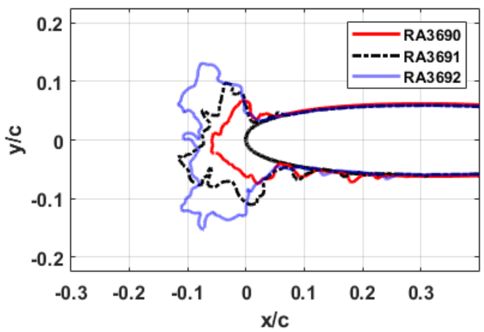

(c) r/R = 0.75

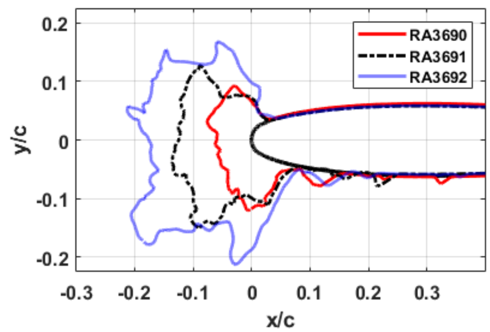

(d) r/R = 0.90

Fig. 11 Effect of Icing Time (n_0 = 0.51)

Table 6 Target Test Conditions for Effect of Icing Time (n_0 = 0.51)

	Target Operating and Cloud Conditions								Similarity Parameters (calculated at r/R = 0.75)				Ice Mass	
Run	V_∞ knots	$t_{\infty,0}$ °C	δ µm	LWC g/m^3	τ min	RPM rev/min	D in	J	n_0^*	A_c	β_0	We_L 10^6	Blade g	Spinner g
RA3690	87	-6.0	15	1.20	1.4	1516	28	2.49	0.51	2.64	0.88	0.15	9.0	12.8
RA3691	"	"	"	"	2.1	"	"	"	"	3.96	"	"	18.7	23.3
RA3692	"	"	"	"	2.8	"	"	"	"	5.28	"	"	28.0	32.3

Figure 12 shows the blade and spinner ice mass as a function of the blade accumulation parameter for both the rime and glaze time sweep. As seen from Fig. 12, both the blade and spinner ice mass appear to increase linearly with time for the rime conditions indicating that there was little change to the total collection efficiencies. For the glaze conditions, the blade ice mass initially increases at the same rate as the rime condition, but then increases at a slightly faster rate after an A_c of ~2.60. It is believed that the increase in the rate of ice mass is due to the formation of features such as horns at these higher accumulation parameters which leads to an increase in the total collection of droplets. A similar trend can also be seen for the spinner ice mass.

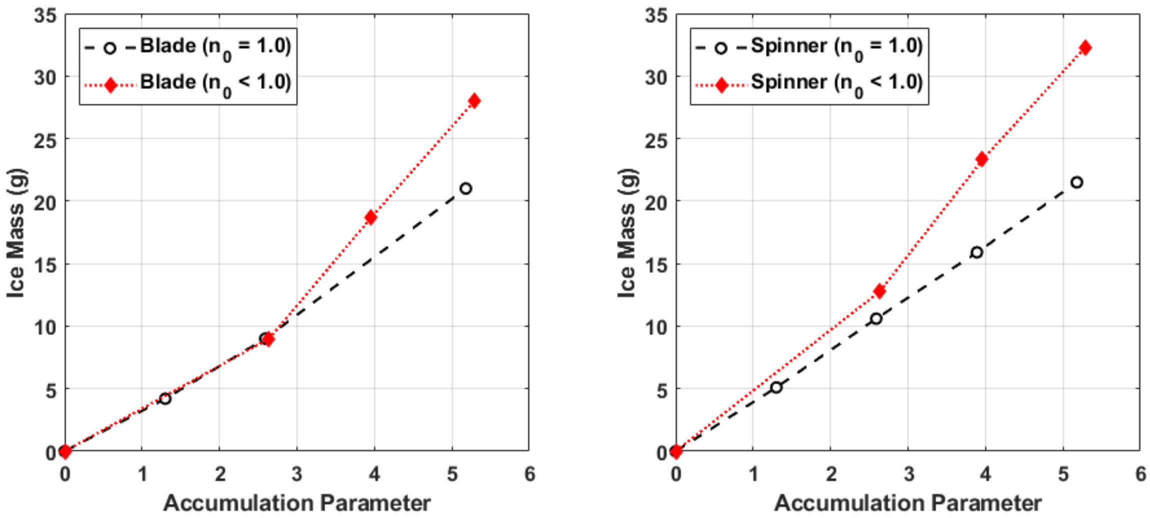

(a) Blade Ice Mass (b) Spinner Ice Mass

Fig. 12 Ice Mass vs Accumulation Parameter for (a) Blade Ice Mass and (b) Spinner Ice Mass

E. Effect of Droplet Diameter

MVD is an important parameter in icing as it affects where the droplets will impinge on the surface. Larger drops, which have higher inertia, are less influenced by the flow field allowing them to fly straighter and impinge farther aft on surfaces. Smaller drops, which have less inertia, tend to follow the flow field and can sometimes be deflected around the airfoil entirely.

Figures 13 and 14 show the effect of varying the MVD between 15, 30, and 80 µm for n_0 = 1.0. Due to facility limitations, the LWC for the 30 MVD run was increased to 0.65 g/m^3 from the nominal 0.55 g/m^3. However, the spray time was reduced accordingly to match A_c and the ice was still considered to be rime at this higher LWC. As seen from Fig. 13, the changes in MVD appeared to have little effect on the main ice shape at these conditions where n_0 = 1.0. However, the lower impingement limits can be seen moving aft when increasing the MVD from 15 to 30 µm. This is more clearly seen in the still images of the high-pressure side of the blade in Fig. 14a and 14b. The increased impingement limits were also accompanied by an increase in the blade ice mass from 9.0 to 11.1 g (a 23% increase) as seen in Fig. 15. The increase in impingement limits and ice mass can be attributed to the increase in β_0 from 88% to 95% when increasing the MVD from 15 to 30 µm. Increasing the MVD from 30 to 80 µm, however, resulted in a much smaller increase in β_0 from 95% to 99% due to the diminishing sensitivity of β_0 to MVD as β_0 approaches 100%. As a result, the change in impingement limits between 30 and 80 µm are much less noticeable and is accompanied by a meager 7% increase in the blade ice mass. The spinner ice mass measurements are also included in Fig. 15 which shows a much greater sensitivity to MVD. Between 15 and 80 MVD, the spinner ice mass increases from 10.6 to 45.3 g (a 327% increase) as compared to an increase in the blade ice mass from 9.0 to 11.9 g (a 32% increase).

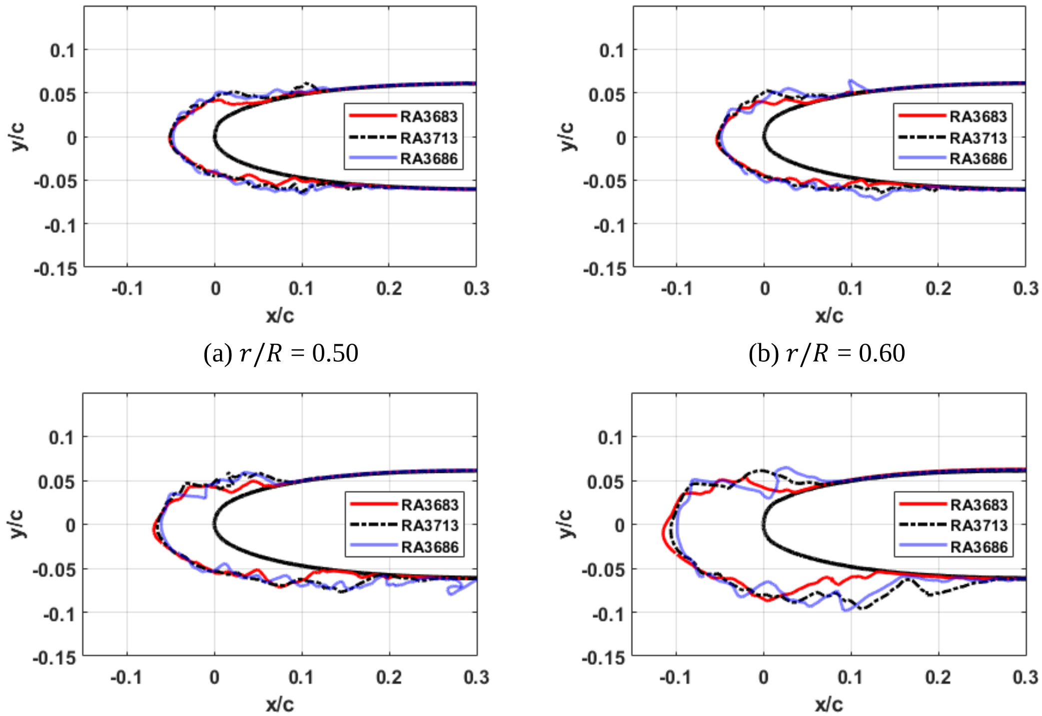

(a) r/R = 0.50 (b) r/R = 0.60

(c) r/R = 0.75 (d) r/R = 0.90

Fig. 13 Effect of MVD

Table 7 Target Test Conditions for Effect of MVD

	Target Operating and Cloud Conditions								Similarity Parameters (calculated at r/R = 0.75)				Ice Mass	
Run	V_∞ knots	$t_{\infty,0}$ °C	δ μm	LWC g/m^3	τ min	RPM rev/min	D in	J	n_0^*	A_c	β_0	We_L 10^6	Blade g	Spinner g
RA3683	87	-15.0	15	0.55	3.0	1516	28	2.49	2.37	2.59	0.88	0.15	9.0	10.6
RA3713	"	"	30	0.65	2.5	"	"	"	1.90	2.55	0.95	"	11.1	28.7
RA3686	"	"	80	0.55	3.0	"	"	"	2.13	2.59	0.99	"	11.9	45.3

(a) 15 MVD (b) 30 MVD (c) 80 MVD

Fig. 14 Ice Accretions on the High-Pressure Side of the Blade Obtained at (a) 15, (b) 30, and (c) 80 MVD corresponding to runs RA3683, RA3713, and RA3686, respectively.

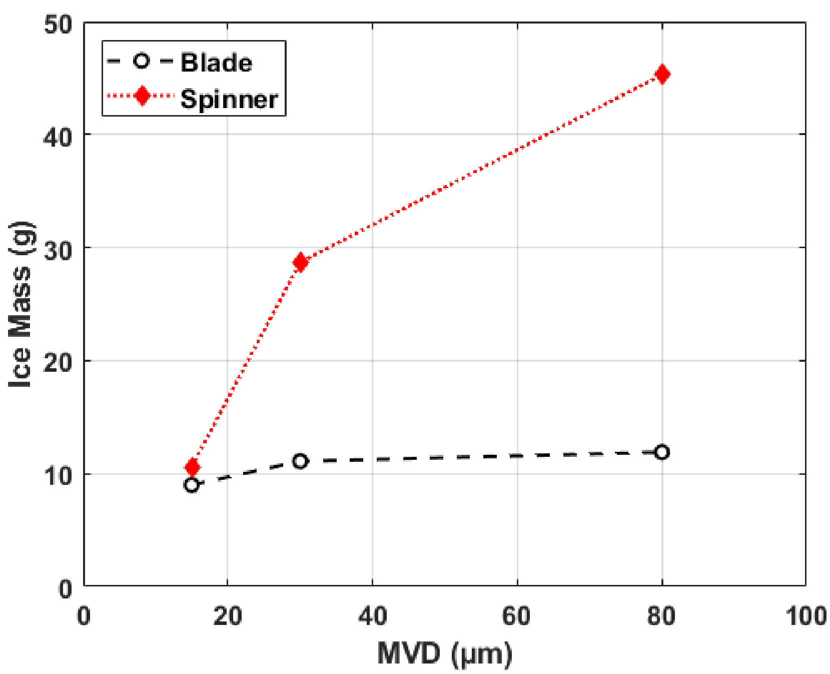

Fig. 15 Blade and Spinner Ice Mass Measurements Obtained at 15, 30, and 80 MVD corresponding to runs RA3683, RA3713, and RA3686, respectively.

The effect of MVD on the impingement limits is also more pronounced on the spinner as shown in Fig. 16 and 17. Note that the conditions for runs RA3711 and RA3712 are identical to runs RA3683 and RA3686, respectively, except for spray time, which was doubled to increase the ice thickness on the spinner to improve the visibility of the impingement limits. The spinner ice mass for runs RA3711 and RA3712 were 21.5 and 92.6 g, respectively. This represents a 330% increase in ice mass on the spinner which is consistent with the 327% increase that was observed between runs RA3683 and RA3686. It is believed that the higher sensitivity of the spinner impingement limits and ice mass to MVD is due to the spinner having a much lower collection efficiency than the propeller over the same range of MVD.

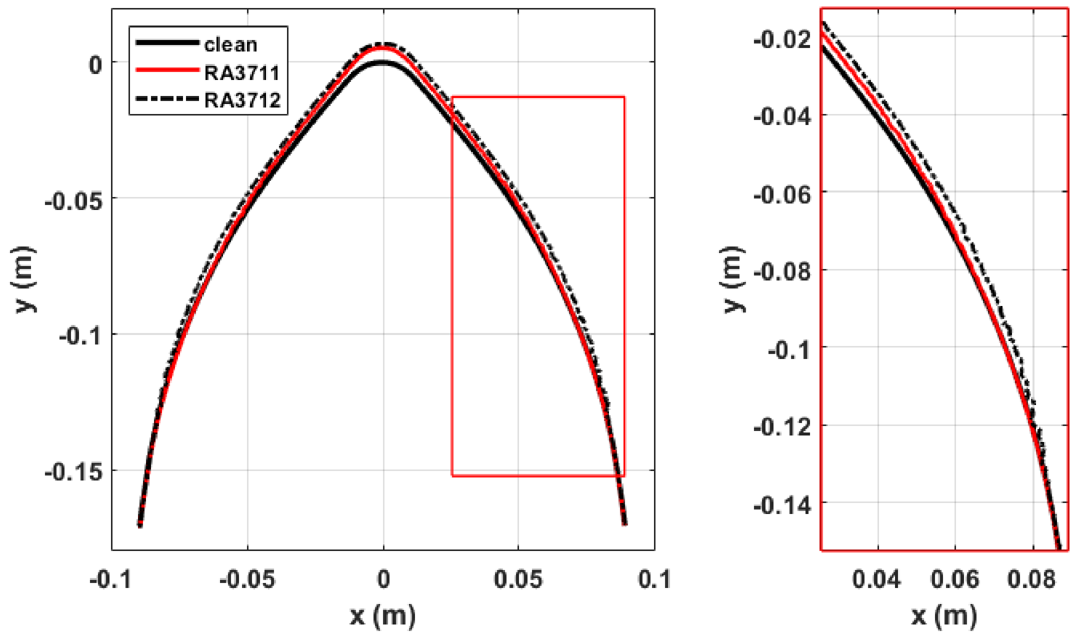

Fig. 16 Spinner Ice Shapes Obtained at 15 and 80 MVD corresponding to runs RA3711 and RA3712, respectively. Conditions for runs RA3711 and RA3712 are identical to runs RA3683 and RA3686 except for spray time, which was doubled to ensure sufficient ice thickness on the spinner.

An interesting phenomenon can be observed in Fig. 17a for the 15 MVD case where narrow regions of high and low droplet concentrations can be seen at the root of the propeller blade. This is similar to the observations by Brun and Dorsch [12] who analyzed the trajectories of water droplets about an ellipsoid of revolution. At 15 MVD, the droplets are deflected around the spinner creating regions of high and low concentrations just outside the spinner surface. At 80 MVD, the droplets are less influenced by the spinner flow field and the droplet concentration is much more uniform as seen in Fig. 17b. This is consistent with the findings from preliminary GlennICE simulations of the propeller and spinner geometry which showed areas of high and low droplet concentrations near the root of the propeller for a particle size of 20 µm but not for a particle size of 80 µm [13]. This could have implications for eVTOL aircraft with air cooling inlets located directly aft of a spinner which may experience blockages due to ice accretion. Clearly, the presence of the spinner flow field must be considered when evaluating the potential for ice to cause blockages in downstream cooling inlets.

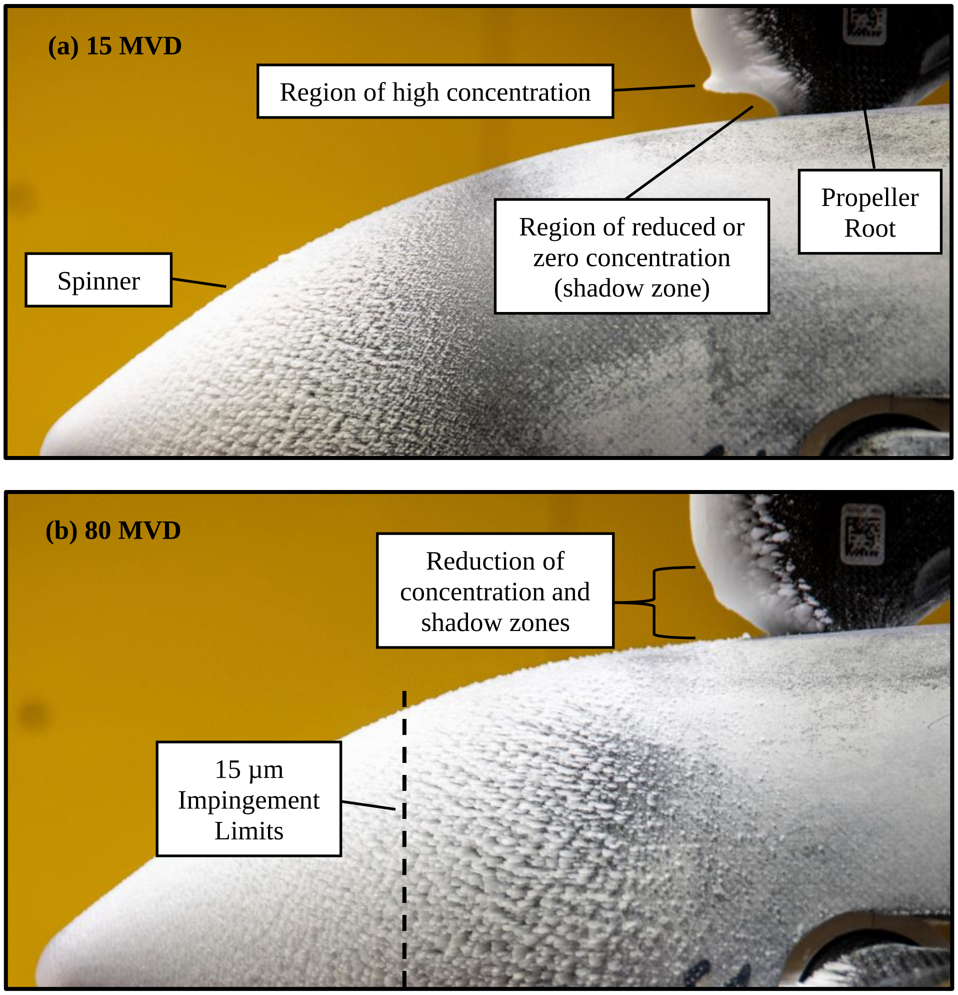

Fig. 17 Side View Images of Spinner Ice Accretions Obtained at (a) 15 and (b) 80 MVD corresponding to runs RA3711 and RA3712, respectively.

F. Effect of LWC

LWC is an important icing parameter as it not only affects the rate of ice accretion, but also the type of ice that forms due to its strong effect on freezing fraction. Figure 18 shows the effect of increasing the LWC from 0.55 to 1.2 g/m^3. All other conditions were held constant, except for spray time, which was reduced for the 1.20 g/m^3 case to match A_c. Temperature was held constant as the analytical value of n_0^* predicted rime along the entire span of the blade for both cases. However, it is clear from Fig. 18 that the freezing fraction for the 1.20 g/m^3 case was not quite unity along the entire span due to the presence of horns. This is consistent with the observation from the temperature sweep in Section 5C that the method for calculating n_0^* was slightly overestimating the true value. Nevertheless, Fig. 18 still shows good agreement between the ice thicknesses at each radial location by matching A_c which suggests a n_0 near unity.

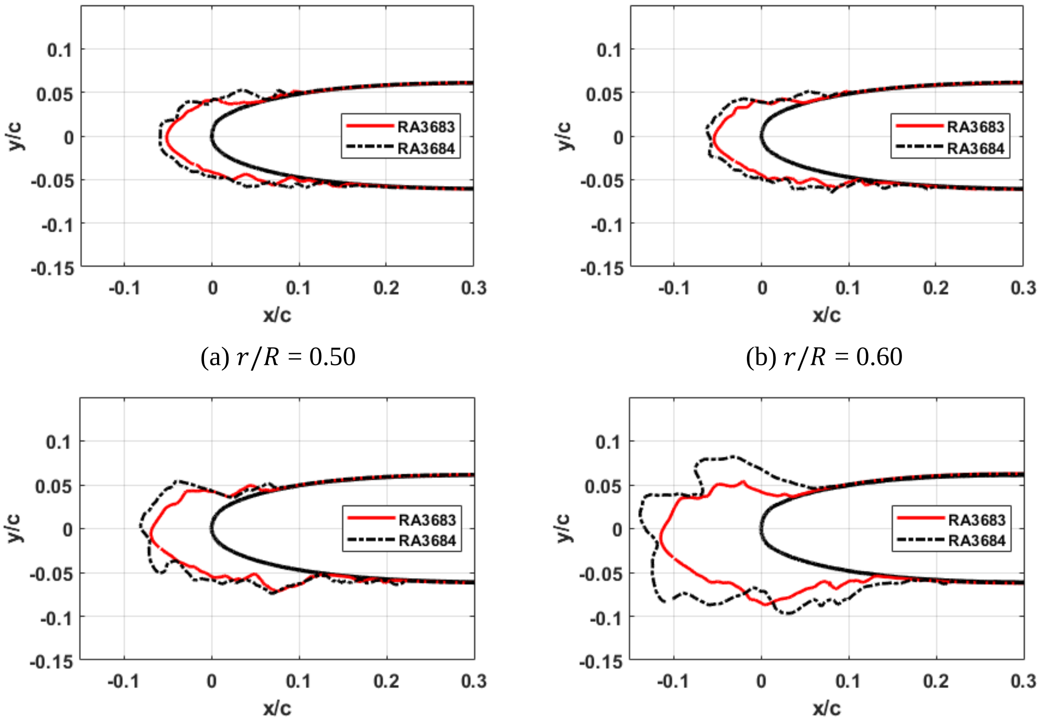

(a) r/R = 0.50 (b) r/R = 0.60

(c) r/R = 0.75 (d) r/R = 0.90

Fig. 18 Effect of Varying LWC (n_0 = 1)

Table 8 Target Test Conditions for Effect of Varying LWC (n_0 = 1)

	Target Operating and Cloud Conditions								Similarity Parameters (calculated at r/R = 0.75)				Ice Mass	
Run	V_∞ knots	$t_{\infty,0}$ °C	δ µm	LWC g/m^3	τ min	RPM rev/min	D in	J	n_0^*	A_c	β_0	We_L 10^6	Blade g	Spinner g
RA3683	87	-15.0	15	0.55	3.0	1516	28	2.49	2.37	2.59	0.88	0.15	9.0	10.6
RA3684	"	"	"	1.20	1.4	"	"	"	1.19	2.64	"	"	12.3	17.1

Another set of conditions were run to assess the impact of varying the LWC between 0.55 and 1.20 g/m^3 at a freezing fraction less than unity. Just as before, the icing time was adjusted to match A_c between both runs. However, the temperature was adjusted this time to maintain the same analytical value of n_0^* = 0.51. As seen from Fig. 19, good agreement between the ice shapes was achieved. This would indicate that the true freezing fraction was very close between both runs even if the analytical freezing fraction may be overestimating the true value. The good agreement between the ice shapes would also suggest that the existing scaling methods developed for fixed-wings may be applicable to rotating airfoils. However, more data over a wider range of conditions is needed to provide more confidence in this approach.

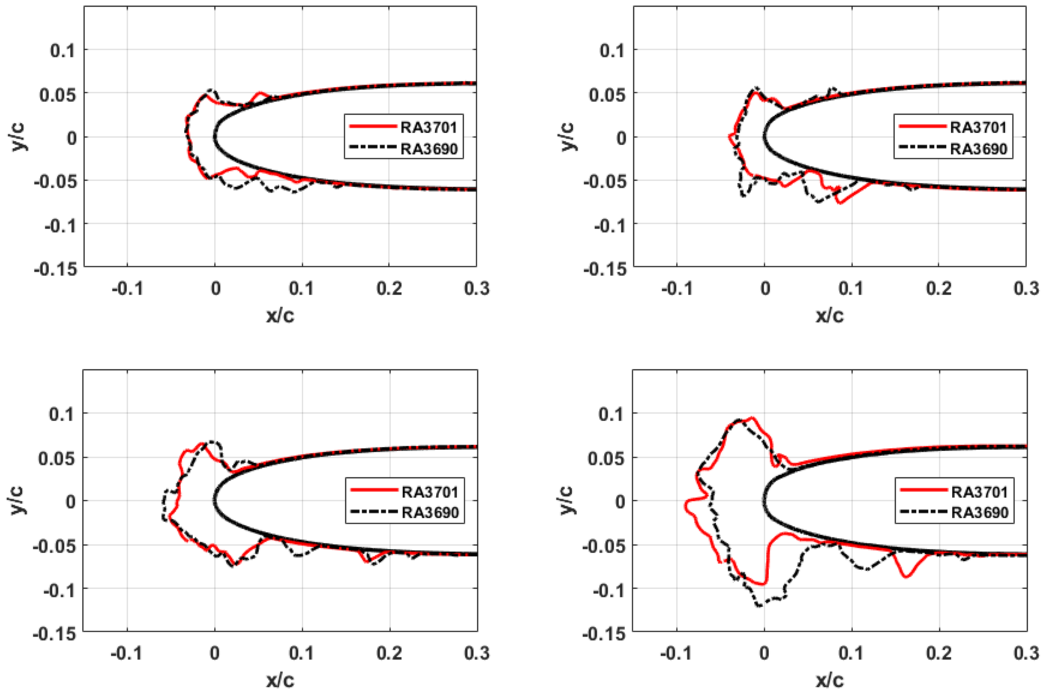

Fig. 19 Effect of Varying LWC (n_0 = 0.51)

Table 9 Target Test Conditions for Effect of Varying LWC (n_0 = 0.51)

	Target Operating and Cloud Conditions								Similarity Parameters (calculated at r/R = 0.75)				Ice Mass	
Run	V_∞ knots	$t_{\infty,0}$ °C	δ µm	LWC g/m^3	τ min	RPM rev/min	D in	J	n_0^*	A_c	β_0	We_L 10^6	Blade g	Spinner g
RA3701	87	-3.0	15	0.55	3.0	1516	28	2.49	0.51	2.59	0.88	0.15	7.0	8.4
RA3690	"	-6.0	"	1.20	1.4	"	"	"	"	2.64	"	"	9.0	12.8

G. Scaling for Propeller Size

When attempting to match ice shapes between two geometrically similar fixed airfoils, V_∞ is found by matching We_L, MVD is found by matching β_0, temperature is found by matching n_0, and icing time is found by matching A_c. While not strictly followed, a similar approach was applied to the propellers in an attempt to match ice shapes on the 24, 28, and 36 inch diameter propellers which are shown in Fig. 20.

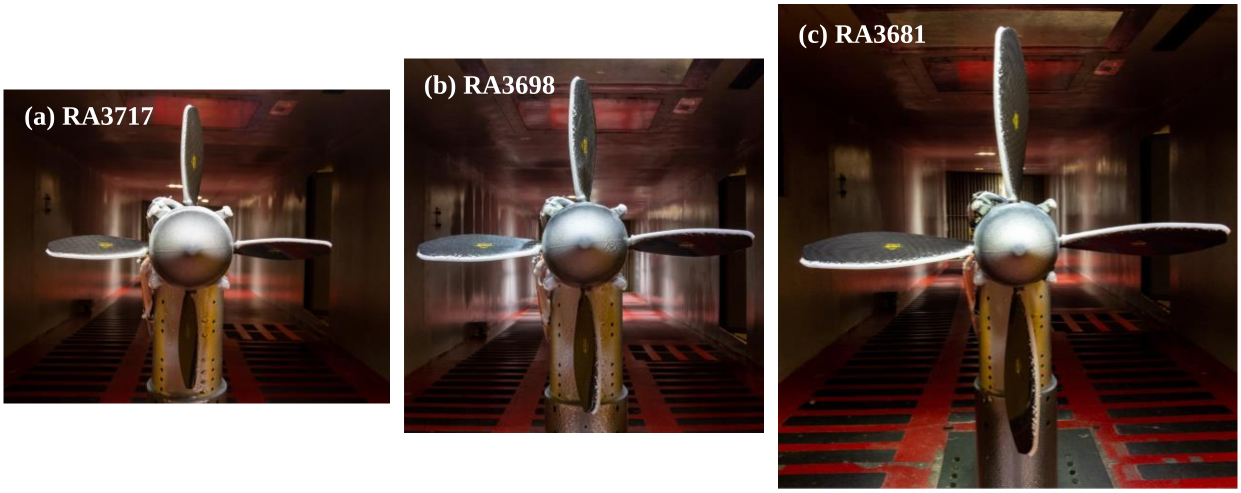

Fig. 20 Post-run images of the (a) 24, (b) 28, and (c) 36 in diameter propellers corresponding to runs RA3717, RA3698, and RA3681, respectively.

As there was found to only be a 4.5% difference in β_0 between the smallest and largest propeller, β_0 was assumed to be approximately equal and so MVD was held constant. Likewise, temperature was held constant as it was believed to be sufficiently cold such that n_0 = 1.0 for each case. Given that n_0 = 1, no attempt at matching We_L was made and V_∞ could therefore be held constant. Propeller RPM was determined by matching advance ratio and each propeller was set to the same target pitch setting. Figure 21 shows the normalized ice shapes after applying the scaling approach described above. As seen from Fig. 21, reasonably good agreement between the ice shapes was achieved.

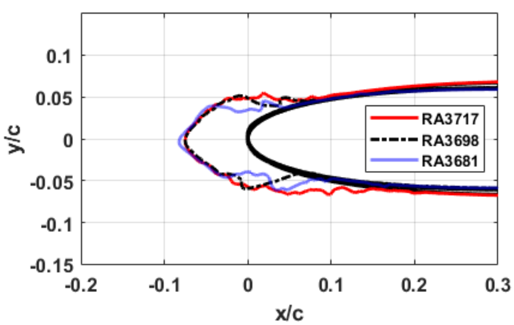

(a) r/R = 0.50

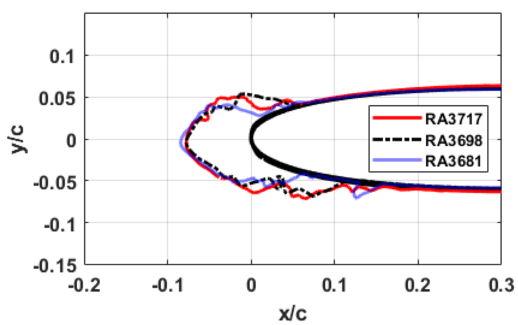

(b) r/R = 0.60

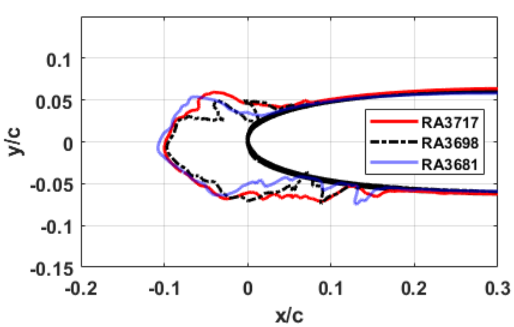

(c) r/R = 0.75

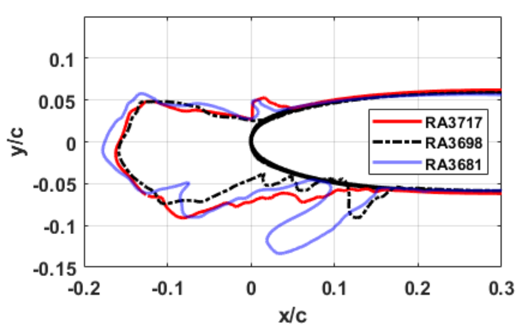

(d) r/R = 0.90

Fig. 21 Scaling for Propeller Size

Table 10 Target Test Conditions for Scaling for Propeller Size

	Target Operating and Cloud Conditions								Similarity Parameters (calculated at r/R = 0.75)				Ice Mass	
Run	V_∞ knots	$t_{\infty,0}$ °C	δ µm	LWC g/m^3	τ min	RPM rev/min	D in	J	n_0^*	A_c	β_0	We_L 10^6	Blade g	Spinner g
RA3717	95	-12.0	15	0.55	3.4	1928	24	2.49	1.95	3.76	0.90	0.15	8.3	14.0
RA3698	"	"	"	"	4.0	1657	28	2.49	1.84	3.78	0.89	0.18	15.1	17.3
RA3681	"	"	"	"	5.0	1300	36	2.47	1.67	3.67	0.86	0.23	28.3	20.8

While the results of the scaling approach are promising, it represents only a single data point under highly idealized conditions. More data is needed to assess the effectiveness of the scaling approach, especially at freezing fractions less than unity where the ice shape is likely to be much more sensitive to temperature and We_L. In addition, demonstration of the scaling methodology over a larger range of propeller sizes is needed to provide greater confidence in the scaling methodology.

VI. Conclusion

A generic, eVTOL propeller was tested in the NASA IRT in an axial flow configuration with the goal of generating ice accretions under well characterized conditions. The data from the test is being used to support the development of the ice prediction code, GlennICE. The primary propeller diameter used was 0.711 m (28 in), however, a 0.610 m (24 in) and 0.914 m (36 in) diameter propeller were also fabricated to explore geometric scaling during a limited portion of the test. A parametric approach was conducted to better understand the relative importance and sensitivity of key icing parameters on the resulting ice accretion. Ice shapes from the test were reviewed for their repeatability, correctness of trends, and sensitivity to parameter variations.

Several repeat conditions were performed which showed excellent ice shape repeatability. The repeat conditions were performed during different times of the day and/or on separate days. The repeat conditions were all performed at rime conditions and more data is needed to assess the repeatability of glaze ice accretions.

A temperature sweep was performed to observe the transition from glaze to rime ice on the propeller. The ice was considered rime once the ice shape appeared to be unaffected by further decreases in temperature. Interestingly, the ice shapes indicated the formation of rime ice much earlier than visual observations which showed a glossy, semi-transparent appearance along the leading edge of the propeller even when the ice shapes appeared to be rime. Glaze ice accretions showed significant spanwise variability as well as the formation of horns which were not observed for the rime ice conditions.

The total ice mass on the propeller blade was found to increase linearly with time for rime conditions. For glaze conditions, the blade ice mass increased at the same rate as the rime conditions up to a certain point. After which, the ice mass increased at a slightly faster rate for the glaze conditions, possibly due to the formation of additional features such as horns. The same trends were also observed for the spinner ice mass.

Varying the MVD appeared to have no effect on the blade main ice shape at rime conditions. More work is needed to assess the impact of MVD on the blade main ice shape for freezing fractions less than unity. Due to the high collection efficiency of the propeller blade, varying the MVD appeared to have only minor effects on the blade impingement limits and total ice mass. The spinner, which is expected to have a significantly lower collection efficiency than the propeller, was much more sensitive to changes in MVD regarding both the impingement limits and ice mass. In addition, the flow field around the spinner was found to produce regions of high and low droplet concentrations near the root of the propeller which could have implications for air cooling inlets located downstream of the spinner.

The key icing similarity parameters calculated at r/R = 0.75 for each run are provided in the paper. The analytical freezing fraction appeared to overestimate the true value of freezing fraction for reasons unknown at this time. The scaling methods developed for unprotected fixed-wing surfaces were explored for use on the propeller with promising results over the range of conditions tested. An attempt to match ice accretions on the 0.610, 0.711, and 0.914 m diameter propellers was made which showed reasonably good agreement between the ice shapes. However, more work is needed to assess the effectiveness of the scaling approach, especially for freezing fractions less than unity. In addition, demonstration of the scaling methodology over a larger range of propeller sizes is needed to provide greater confidence in the scaling methodology.

Acknowledgments

The authors would like to acknowledge all of those who helped make this a successful test. In particular, the authors would like to thank Keith Hunker, Xavier Collazo Fernandez, Joe Wisniewski, and Scott Hensley for their invaluable technical support. The authors would also like to thank Jordan Salkin and Quentin Schwinn for their imaging support during testing. In addition, this work could not have been possible without the support of the NASA Glenn Icing Branch and the IRT engineers and technicians for their efforts in making this test campaign a success. The experimental work presented in this paper was funded by NASA's Revolutionary Vertical Lift and Technology project.

References

[1] Garrow, L. A., German, B., Schwab, N. T., Patterson, M. D., Mendonca, N., Gawdiak, Y. O. and Murphy, J. R., "A Proposed Taxonomy for Advanced Air Mobility," *AIAA AVIATION 2022 Forum*, AIAA Paper 2022-3321, Chicago, IL, June-July 2022. doi: 10.2514/6.2022-3321

[2] Whiteside, S. K. S., Pollard, B. P., Antcliff, K. R., Zawodny, N. S., Fei, X., Silva, C., and Medina, G. L., "Design of a Tiltwing Concept Vehicle for Urban Air Mobility," NASA/TM-20210017971, 2021.

[3] Federal Aviation Administration, "Airworthiness Criteria: Special Class Airworthiness Criteria for the Joby Aero, Inc. Model JAS4-1 Powered-Lift," *Federal Registrar*, Vol. 89, No. 47, 2024, pp. 17230, 17264.

[4] Federal Aviation Administration, "Airworthiness Criteria: Special Class Airworthiness Criteria for the Archer Aviation, Inc. Model M001 Powered-Lift," *Federal Registrar*, Vol. 89, No. 102, 2024, pp. 45944, 45977.

[5] Porter, C., Potapczuk, M., Ozoroski, T., Sabri, Z., Galloway, E., Rigby, D., Wright, W., and Tsao. P., 2024. "GlennICE Manual 4.1.0." NASA/TM-20240002191, 2024.

[6] Rigby, D. L. and von Hardenberg, P. H., "GlennICE Simulation of 24, 28, and 36 Inch Diameter eVTOL Propellers in Forward Flight," *AIAA AVIATION 2024 Forum*, Las Vegas, NV, July-August 2024.

[7] Zawodny, N. S., Pettingill, N. A., Lopes, L. V., and Ingraham, D, J., "Experimental Validation of an Acoustically and Aerodynamically Optimized UAM Proprotor Part 1: Test Setup and Results," NASA/TM-20220015637, 2023.

[8] Soeder, R. H., Sheldon, D. W., Ide, R. F., Spera, D. A., and Andracchio, C. R., "NASA Glenn Icing Research Tunnel User Manual," NASA/TM-2003-212004, 2003.

[9] Timko, E. N., King-Steen, L. E., Van Zante, J. F., and Acosta, W. J., "NASA Glenn Icing Research Tunnel: 2019 Cloud Calibration Procedure and Results," NASA/TM-20205009045, 2021.

[10] Anderson, D. N., "Manual of Scaling Methods," NASA/CR-2004-212875, 2004.

[11] Anderson, D. N. and Tsao, J., "Ice Shape Scaling for Aircraft in SLD Conditions," NASA/CR-2008-215302, 2008.

[12] Brun, R. J. and Dorsch, R. G., "Variation of Local Liquid-Water Concentration about an Ellipsoid of Fineness Ratio 10 Moving in a Droplet Field," NACA-TN-3410, 1955.

[13] Rigby, D. L., and von Hardenberg, P. H., "Demonstration of Initial GlennICE Relative Frame Capability: Axial-Flow Propeller", SAE International Icing Conference, 23ICE-0029/2023-01-1457, 2023.
doi: 10.4271/2023-01-1457